Control Interaction Modeling and Analysis of Grid-Forming Battery Energy Storage System for Offshore Wind Power Plant

Zhao, Fangzhou; Wang, Xiongfei; Zhou, Zichao; Harnefors, Lennart; Svensson, Jan R.; Kocewiak, Lukasz Hubert; Gryning, Mikkel Peter Sidoroff

Published in:
IEEE Transactions on Power Systems

DOI (link to publication from Publisher):
10.1109/TPWRS.2021.3096850

Publication date:
2022

Document Version
Accepted author manuscript, peer reviewed version

Control Interaction Modeling and Analysis of Grid-Forming Battery Energy Storage System for Offshore Wind Power Plant

Fangzhou Zhao, *Member, IEEE*, Xiongfei Wang, *Senior Member, IEEE*, Zichao Zhou, *Student Member, IEEE*, Lennart Harnefors, *Fellow, IEEE*, Jan R. Svensson, *Senior Member, IEEE*, Łukasz Hubert Kocewiak, *Senior Member, IEEE*, and Mikkel Peter Sidoroff Gryning

***Abstract*—With the increasing deployment of offshore wind power plants (WPPs), the grid-forming (GFM) battery energy storage system (BESS) has recently emerged as an attractive solution to improve the dynamic performances of WPPs. However, the control interactions of the GFM-BESS and offshore WPP, under different grid strengths, tend to complicate the controller-parameter tuning. This paper presents a modeling method for analyzing control interactions of offshore WPP and GFM-BESS, which sheds clear insights into the critical controller parameters to the system dynamics. Differing from conventional methods, a frequency-domain model of GFM-BESS, obtained by taking the Laplace transform of the corresponding state-space model, is developed first. This allows the impedance model of offshore WPP, including a black-box model of long transmission cable, to be flexibly integrated. Based on the model, both closed-loop transfer-function and pole-based dynamic analyses are then performed. Electromagnetic transient simulations corroborate the effectiveness of the model and analysis.**

***Index Terms*—battery energy storage system (BESS), control interaction, grid-forming, offshore wind power plant (WPP)**

I. Introduction

THE burgeoning offshore wind power plants (WPPs) have posed challenges to the reliable operation of power systems and, particularly the offshore WPPs that are connected through long underground and submarine cables to the onshore grid, e.g., Horns II in Denmark [1]. The dynamic interactions of wind turbines (WTs) can induce undesirable harmonics, resonances and instability issues due to the long medium- and high-voltage alternating current cables [2], [3].

To improve the dynamic performance of offshore WPPs, the static synchronous compensator (STATCOM) is widely used in offshore WPPs [4], [5]. The STATCOM can provide reactive power and voltage regulation [6] as well as resonance damping for WPPs [7]. Nevertheless, it is unable to perform the active power-related services, e.g., to smoothen the power fluctuation of WPPs [8]. Thus, the STATCOM with battery energy storage system (BESS) is recently introduced in [9], [10], featuring both active and reactive power controllability. However, in offshore WPPs, the long power transmission cables may result in a low short-circuit ratio (SCR) at the WT terminals. The negative damping of phase-locked loop (PLL) in WTs will destabilize the system [11] as the increase of the installed WPP capacity.

To mitigate the instability issue of WPPs in weak grids, the STATCOM-BESS that is equipped by the grid-forming (GFM) control, referred to GFM-BESS hereafter, is recently introduced [12]–[14]. In contrast to the PLL-synchronized STATCOM, the GFM-BESS not only can operate stably in ultra-weak grids [15], but provides also more services, e.g., black-start capability and inertial responses [16], [17]. Several studies have reported the stability and control analysis of GFM-BESS [14], [18], [19]. It is proved in [14] that the GFM-BESS equivalently enhances the grid stiffness for wind farms in virtue of its inductive impedance characteristic, which is helpful to suppress the sub-synchronous resonance (SSR). However, the existing research focused more on the GFM-BESS itself [18], [19] or SSR damping [14], rather than the interactions analysis revealing the closed-loop dynamic behaviors for the offshore WPPs and GFM-BESS. Yet, unknown control interactions of GFM-BESS and offshore WPP may still lead to undesired oscillations under certain grid conditions.

To do so, the small-signal models of the overall system including controller details should be built first. The modeling methods can be categorized into four groups, which are 1) impedance-based model [20]–[22], 2) the state-space model [23], [24], 3) the component connection method (CCM) [25], [26], and 4) closed-loop transfer function model [27], [28].

The impedance-based model can effectively predict the system stability at the terminals of the subsystems including black box models based on generalized Nyquist criterion [21]. However, the impedance models are all relied on the terminal voltage-current relations, which works well with stability analysis yet fails to characterize closed-loop responses of power control loops. As for the state-space model, it is commonly used in the white-box system stability analysis, which provides insight on oscillation modes of the whole system [23]. However, the derivation of large-scale WPPs is computationally intensive and complicated. Hence, the CCM is increasingly used to derive the state-space model [25], [26]. The CCM combines the state-space model of each subsystem based on interconnection matrix to reduce the computational effort. However, most controllers are initially designed in the form of transfer functions, such as low-pass filters [29] and virtual resistance [30] in GFM control. They should be transformed into the time domain to be

integrated into the state-space model. Further, the extension of CCM model, e.g., different control structures, is non-trivial, due to the cross couplings of control loops [26]. The final method, closed-loop transfer function model [27], is a straight-forward way to design the controllers based on the reference-to-output dynamic analysis. Nevertheless, most of them focus on the modeling of one converter with the dedicated control, rather than a more generalized method that can be used to identify the interactions between different components in a large-scale system, i.e., grid, GFM-BESS and offshore WPPs.

This paper thus proposes a modeling and analysis method to identify the control interactions and dynamic behaviors for the GFM-BESS usage in high-power offshore WPPs. First, a transfer-function-based model is developed from Laplace transform of a time-domain state-space open-loop plant, which not only simplifies the formulation of closed-loop transfer function matrix, but also facilitates the integration of black-box cable models. Then, two types of interaction analyses are presented for the GFM-BESS and offshore WPPs, i.e., 1) the assessments of the closed-loop control bandwidth and coupling effect of power control loops, which are based on the frequency response of reference-to-output transfer function matrix, and 2) the dynamic behaviors evaluation of critical controller parameters and different SCRs of the grid, which are based on the sensitivity analysis. The simulation results prove the effectiveness of the proposed modeling method and analysis.

II. System Description and Modeling Method

A. System description and assumptions

The diagram of an offshore WPP system with GFM-BESS is depicted in Fig. 1. The system is simplified from a practical case – Horns II project [1]. The 400 MW offshore WPP connects to the onshore point of common coupling (PCC) via underground and submarine cables with shunts for reactive power compensation. The onshore grid impedance is denoted by inductance L_g. A 112 MVA GFM-BESS with 50 MW battery packs installed at the DC-link supports the voltage and frequency at the PCC. To focus on the studies of GFM and PLL features, the following assumptions are made:

1) The WPPs are represented by an aggregated 400 MW PLL-synchronized grid-following (GFL) [25], [31] converter shown in Fig. 1 for simplicity, since the differences of WTs are comparatively small. The *LC* output filter is used.
2) The studied GFM dynamics are mainly in low-frequency range due to the low bandwidth of outer loops [29]. Hence, the *L* output filter is modeled [27], [30] in GFM-BESS irrespective of different topologies for simplicity.

The detailed control diagrams of GFM-BESS and GFL-WPPs will be shown in Section III and IV.

B. Modeling method and system partitioning

To analyze the control interactions, the small-signal model needs to be developed step-by-step. Therefore, the flow chart of the proposed modeling method is presented in Fig. 2.

First, the system is partitioned into two subsystems at the PCC as shown in Fig. 1. The subsystem I represents the GFM-BESS, which will be modeled based on transfer function matrices. The inputs of the model of subsystem I preserve the control references and PCC terminal voltages. The subsystem II contains the grid impedance, shunts, cables, transformers and WPP, which will be modeled as an equivalent impedance that characterizes the voltage-to-current behaviors. Hence, the two subsystems are modeled separately and then integrated together based on the PCC terminal voltage and current relations. In this way, the closed-loop GFM control dynamic performances can be explicitly captured with the interacted WPP under different grid conditions.

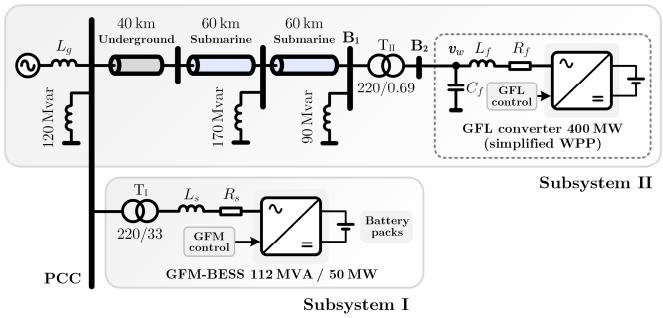

Fig. 1. Diagram of a simplified offshore WPP system with GFM-BESS.

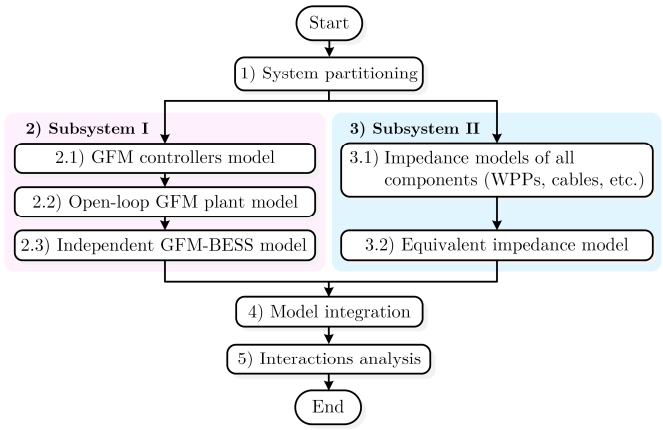

Fig. 2. Flow chart of the small-signal modeling approach.

The rest of the paper will follow the modeling steps in Fig. 2.

III. Subsystem I – Transfer Function-Based Modeling of GFM-BESS

A. GFM controller model

According to Fig. 2, the GFM-BESS will be modeled first in step 2.1). Fig. 3 shows the GFM control diagram, including the power synchronization control (PSC) [27], reactive power control (RPC), alternating voltage control (AVC) [29], and virtual resistance (VR) [30]. The output voltage is sampled at the high-voltage (HV) side of the transformer, which is modeled as the leakage inductance L_l and resistance R_l [32] in Fig. 3 for simplicity. The inner current control is designed for current limitation, which is only activated when the references exceed the limits in faults [29]. In normal operation (small-signal analysis), the current control is transparent and shows no influence [30], thus is neglected in Fig. 3. Focusing on the outer loops with VR, the transfer functions $C_P(s)$, $C_Q(s)$ and $C_V(s)$ denote the expressions of controllers, which can be

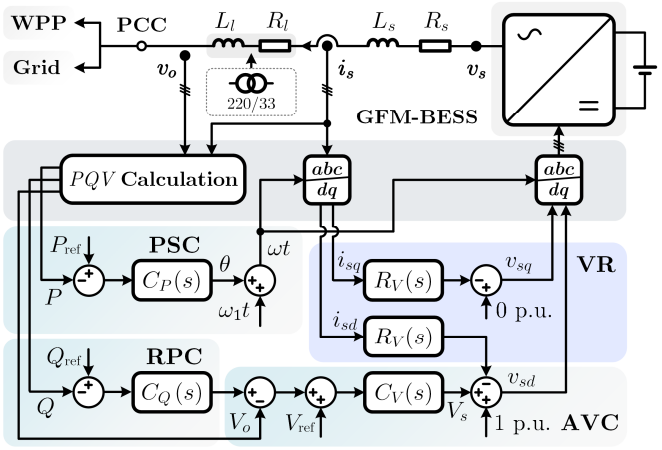

Fig. 3. Control diagram of the GFM-BESS.

flexibly adjusted for different functions, such as with or without inertia. Besides, the outer loop bandwidth is quite low, hence the delays of GFM-BESS are not modeled in this study [29], [30]. Then, the controller model of PSC is first derived as

$$\hat{\theta} = C_P(s)\left(\hat{P}_{\text{ref}} - \hat{P}\right) \tag{1}$$

where

$$C_P(s) = \frac{k_{si}}{s}\frac{\omega_p}{s+\omega_p}. \tag{2}$$

The variables with a hat, e.g., the control voltage angle $\hat{\theta}$ and active power $\hat{P}$, represent the small-signal perturbations. k_{si} denotes the integral gain or the so-called droop value. A low-pass filter (LPF) with cut-off frequency ω_p is normally applied to filter the calculated instantaneous active power. Next, the linearized dynamics of cascaded RPC and AVC are modeled as

$$\hat{V}_s = C_V(s)\left(\hat{V}_{\text{ref}} - \hat{V}_o\right) + C_V(s)C_Q(s)\left(\hat{Q}_{\text{ref}} - \hat{Q}\right) \tag{3}$$

where

$$C_V = \frac{k_{ei}}{s}\frac{\omega_v}{s+\omega_v},\ C_Q = k_q\frac{\omega_q}{s+\omega_q}. \tag{4}$$

$\hat{V}_s$ denotes the magnitude perturbation of control voltage. The RPC and AVC also apply the LPFs for the calculated reactive power $\hat{Q}$ and voltage magnitude $\hat{V}_o$. k_{ei} denotes the integral gain of AVC. k_q is the proportional gain of RPC, while it is set as 0 in this case for simplicity. Then, the controller models (1) and (3) can be organized into a matrix form as follows for easier integration in the following step 2.3).

$$\hat{\boldsymbol{u}}_{\boldsymbol{\theta V}} = \boldsymbol{G}_{\boldsymbol{c}}(s)\left(\hat{\boldsymbol{u}}_{\mathbf{ref}} - \hat{\boldsymbol{y}}\right) \tag{5}$$

where

$$\begin{aligned}
&\hat{\boldsymbol{u}}_{\boldsymbol{\theta V}} = \begin{bmatrix}\hat{\theta} & \hat{V}_s\end{bmatrix}^T,\ \hat{\boldsymbol{y}} = \begin{bmatrix}\hat{P} & \hat{Q} & \hat{V}_o\end{bmatrix}^T,\\
&\hat{\boldsymbol{u}}_{\mathbf{ref}} = \begin{bmatrix}\hat{P}_{\text{ref}} & \hat{Q}_{\text{ref}} & \hat{V}_{\text{ref}}\end{bmatrix}^T,\\
&\boldsymbol{G}_{\boldsymbol{c}}(s) = \begin{bmatrix}C_P(s) & 0 & 0\\ 0 & C_V(s)C_Q(s) & C_V(s)\end{bmatrix}.
\end{aligned} \tag{6}$$

In (5), $\hat{\boldsymbol{u}}_{\boldsymbol{\theta V}}$ denotes the vector of the controller outputs, $\hat{\boldsymbol{u}}_{\mathbf{ref}}$ is the vector of input references, and $\hat{\boldsymbol{y}}$ is the vector of GFM-BESS system outputs. These variables are all in the *s*-domain.

B. Open-loop GFM plant model

It is known that the GFM control regulates the magnitude and angle of the control voltage v_s. Hence, in *dq* frame, the small-signal perturbations of GFM control voltages in time-domain $\hat{v}_{sd}(t)$ and $\hat{v}_{sq}(t)$ can be linearized as [27]

$$\begin{bmatrix}\hat{v}_{sd}(t)\\ \hat{v}_{sq}(t)\end{bmatrix} = \boldsymbol{B}_{\boldsymbol{s}}\hat{\boldsymbol{u}}_{\boldsymbol{\theta V}}(t) \tag{7}$$

where

$$\boldsymbol{B}_{\boldsymbol{s}} = \begin{bmatrix}-V_{s0}\sin\theta_0 & \cos\theta_0\\ V_{s0}\cos\theta_0 & \sin\theta_0\end{bmatrix},\ \hat{\boldsymbol{u}}_{\boldsymbol{\theta V}}(t) = \begin{bmatrix}\hat{\theta}(t)\\ \hat{V}_s(t)\end{bmatrix}. \tag{8}$$

The subscript that includes "0" indicates the steady-state value of the variable. Then, the small-signal model of the open-loop control in *dq* frame is expressed as

$$\begin{aligned}
L_{eq}\frac{\mathrm{d}\hat{i}_{sd}(t)}{\mathrm{d}t} &= -R_{eq}\hat{i}_{sd}(t) + \omega_1 L_{eq}\hat{i}_{sq}(t) + \hat{v}_{sd}(t) - \hat{v}_{od}(t)\\
L_{eq}\frac{\mathrm{d}\hat{i}_{sq}(t)}{\mathrm{d}t} &= -R_{eq}\hat{i}_{sq}(t) - \omega_1 L_{eq}\hat{i}_{sd}(t) + \hat{v}_{sq}(t) - \hat{v}_{oq}(t)
\end{aligned} \tag{9}$$

where

$$L_{eq} = L_s + L_l,\ R_{eq} = R_s + R_l,\ \omega_1 = 314\ \text{p.u.} \tag{10}$$

The per-unit values in TABLE I are used for (9), where the base frequency is $\omega_{\text{base}} = 1$ rad/s. The output voltage is the high-voltage side of the transformer in Fig. 3. Thus, the equivalent transformer leakage inductance L_l and resistance R_l [32] should be added with the filters in the model. Next, substituting (7) into (9), the open-loop GFM plant in time-domain state-space is

$$\begin{aligned}
\frac{\mathrm{d}\hat{\boldsymbol{x}}(t)}{\mathrm{d}t} &= \boldsymbol{A}_{\boldsymbol{p}}\hat{\boldsymbol{x}}(t) + \frac{1}{L_{eq}}\begin{bmatrix}\boldsymbol{B}_{\boldsymbol{s}} & -\boldsymbol{I}_{2\times 2}\end{bmatrix}\begin{bmatrix}\hat{\boldsymbol{u}}_{\boldsymbol{\theta V}}(t)\\ \hat{\boldsymbol{u}}_{\boldsymbol{v}}(t)\end{bmatrix}\\
\hat{\boldsymbol{y}}(t) &= \boldsymbol{C}\hat{\boldsymbol{x}}(t) + \boldsymbol{D}\hat{\boldsymbol{u}}_{\boldsymbol{v}}(t)
\end{aligned} \tag{11}$$

where

$$\begin{aligned}
&\hat{\boldsymbol{x}}(t) = \begin{bmatrix}\hat{i}_{sd}(t) & \hat{i}_{sq}(t)\end{bmatrix}^T,\ \hat{\boldsymbol{u}}_{\boldsymbol{v}}(t) = \begin{bmatrix}\hat{v}_{od}(t) & \hat{v}_{oq}(t)\end{bmatrix}^T,\\
&\hat{\boldsymbol{y}}(t) = \begin{bmatrix}\hat{P}(t) & \hat{Q}(t) & \hat{V}_o(t)\end{bmatrix}^T,\\
&\boldsymbol{A}_{\boldsymbol{p}} = \frac{1}{L_{eq}}\begin{bmatrix}-R_{eq} & \omega_1 L_{eq}\\ -\omega_1 L_{eq} & -R_{eq}\end{bmatrix},\ \boldsymbol{I}_{2\times 2} = \begin{bmatrix}1 & 0\\ 0 & 1\end{bmatrix},\\
&\boldsymbol{C} = \begin{bmatrix}v_{od0} & v_{oq0}\\ v_{oq0} & -v_{od0}\\ 0 & 0\end{bmatrix},\ \boldsymbol{D} = \begin{bmatrix}i_{sd0} & i_{sq0}\\ -i_{sq0} & i_{sd0}\\ v_{od0}/V_{o0} & v_{oq0}/V_{o0}\end{bmatrix}.
\end{aligned} \tag{12}$$

$\hat{\boldsymbol{u}}_{\boldsymbol{\theta V}}(t)$ is already given in (8). (11) is a typical time-domain state-space model. The states are output currents, and the inputs are output voltages, magnitude and angle of control voltages. To facilitate the integration of *s*-domain models including the controllers, performing Laplace transform [32], [33] to (11) with the zero-initial state, $\hat{\boldsymbol{x}}(t=0) = 0$, yields

$$\begin{aligned}
s\hat{\boldsymbol{x}} &= \boldsymbol{A}_{\boldsymbol{p}}\hat{\boldsymbol{x}} + \frac{1}{L_{eq}}\begin{bmatrix}\boldsymbol{B}_{\boldsymbol{s}} & -\boldsymbol{I}_{2\times 2}\end{bmatrix}\begin{bmatrix}\hat{\boldsymbol{u}}_{\boldsymbol{\theta V}}\\ \hat{\boldsymbol{u}}_{\boldsymbol{v}}\end{bmatrix}\\
\hat{\boldsymbol{y}} &= \boldsymbol{C}\hat{\boldsymbol{x}} + \boldsymbol{D}\hat{\boldsymbol{u}}_{\boldsymbol{v}}
\end{aligned} \tag{13}$$

where

$$\hat{\boldsymbol{x}} = \begin{bmatrix}\hat{i}_{sd} & \hat{i}_{sq}\end{bmatrix}^T,\ \hat{\boldsymbol{u}}_{\boldsymbol{v}} = \begin{bmatrix}\hat{v}_{od} & \hat{v}_{oq}\end{bmatrix}^T. \tag{14}$$

$\hat{\boldsymbol{u}}_{\boldsymbol{\theta V}}$ and $\hat{\boldsymbol{y}}$ is already given in (6). The variables $\hat{\boldsymbol{x}}$, $\hat{\boldsymbol{u}}_{\boldsymbol{\theta V}}$, $\hat{\boldsymbol{u}}_{\boldsymbol{v}}$ and $\hat{\boldsymbol{y}}$ are all in the *s*-domain. Please note that the argument "(s)", e.g., $\hat{\boldsymbol{x}}(s)$, is omitted for simplification.

Then, consider the virtual resistance, which can be regarded as a part of the plant, i.e., an additional resistance to R_{eq} in $\boldsymbol{A}_{\boldsymbol{p}}$ [29] as (13) is already in *s*-domain, yielding

$$\begin{aligned} s\hat{\boldsymbol{x}} &= \boldsymbol{A}_{\boldsymbol{pv}}(s)\hat{\boldsymbol{x}} + \frac{1}{L_{eq}}[\boldsymbol{B}_{\boldsymbol{s}} \quad -\boldsymbol{I}_{2\times 2}]\begin{bmatrix}\hat{\boldsymbol{u}}_{\boldsymbol{\theta V}}\\ \hat{\boldsymbol{u}}_{\boldsymbol{v}}\end{bmatrix} \\ \hat{\boldsymbol{y}} &= \boldsymbol{C}\hat{\boldsymbol{x}} + \boldsymbol{D}\hat{\boldsymbol{u}}_{\boldsymbol{v}} \end{aligned} \tag{15}$$

where

$$\begin{aligned} \boldsymbol{A}_{\boldsymbol{pv}}(s) &= \frac{1}{L_{eq}}\begin{bmatrix} -R_{eq} - R_V(s) & \omega_1 L_{eq} \\ -\omega_1 L_{eq} & -R_{eq} - R_V(s)\end{bmatrix}, \\ R_V(s) &= \frac{sR_a}{s+\alpha_c}. \end{aligned} \tag{16}$$

The VR in (16) is realized by a proportional gain R_a with a high-pass filter (HPF) for power resonance damping near 50 Hz [29]. α_c denotes the cut-off frequency of the HPF, which can be chosen as 31.4~62.8 rad/s [30].

C. Independent GFM-BESS model

The outputs $\hat{\boldsymbol{u}}_{\boldsymbol{\theta V}}$ of the controller model in (5) are the inputs of the open-loop state-space model (15). Hence, by inserting (5) into (15) gives

$$\begin{aligned} s\hat{\boldsymbol{x}} &= \boldsymbol{A}_{\mathbf{GFM}}(s)\hat{\boldsymbol{x}} + \boldsymbol{B}_{\mathbf{GFM}}(s)\begin{bmatrix}\hat{\boldsymbol{u}}_{\mathbf{ref}}\\ \hat{\boldsymbol{u}}_{\boldsymbol{v}}\end{bmatrix} \\ \hat{\boldsymbol{y}} &= \boldsymbol{C}\hat{\boldsymbol{x}} + \boldsymbol{D}\hat{\boldsymbol{u}}_{\boldsymbol{v}} \end{aligned} \tag{17}$$

where

$$\begin{aligned} \boldsymbol{A}_{\mathbf{GFM}}(s) &= \boldsymbol{A}_{\boldsymbol{pv}}(s) - \frac{1}{L_{eq}}\boldsymbol{B}_s(s)\boldsymbol{G}_{\boldsymbol{c}}(s)\boldsymbol{C}, \\ \boldsymbol{B}_{\mathbf{GFM}}(s) &= \frac{1}{L_{eq}}[\boldsymbol{B}_{\boldsymbol{s}}\boldsymbol{G}_{\boldsymbol{c}}(s) \quad -\boldsymbol{I}_{2\times 2} - \boldsymbol{B}_{\boldsymbol{s}}\boldsymbol{G}_{\boldsymbol{c}}(s)\boldsymbol{D}]. \end{aligned} \tag{18}$$

$\hat{\boldsymbol{u}}_{\mathbf{ref}}$ and $\hat{\boldsymbol{y}}$ are given in (6), $\hat{\boldsymbol{x}}$ and $\hat{\boldsymbol{u}}_{\boldsymbol{v}}$ are given in (12). Please note that (17) is still an independent GFM-BESS model, since it preserves the PCC terminal voltages $\hat{\boldsymbol{u}}_{\boldsymbol{v}}$ as inputs, thus the dynamics of subsystem II are not included yet. The final integration will be presented in Section V. The coefficient matrices in (15) and (17) $\boldsymbol{A}_{\boldsymbol{pv}}(s)$, $\boldsymbol{A}_{\mathbf{GFM}}(s)$ and $\boldsymbol{B}_{\mathbf{GFM}}(s)$ are high-order *s*-domain transfer functions. Hence, the models (15) and (17) are actually based on the transfer function matrices, which distinguishes from the traditional time-domain state-space model (11). The output currents are explicit, whereas other states are implicit in the model. In this way, the *s*-domain controllers (5) can be flexibly integrated into the model, saving the computational effort to transform them into time-domain and derive the high-dimensional constant matrices.

IV. Subsystem II – Impedance Modeling

A. Impedance modeling of all components

In the step 3.1), all the components in the subsystem II are modeled as impedances or admittances. They can be divided into 4 types:

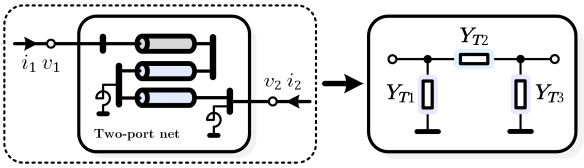

Fig. 4. Black-box modeling of the long cables network.

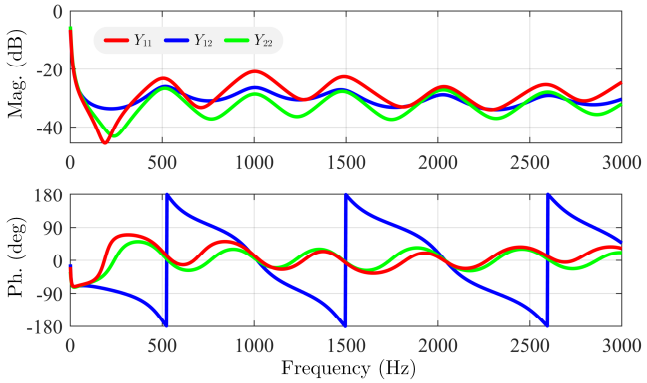

Fig. 5. Bode plots of the PI-section model of long cables network.

1) Grid impedance ($\omega_1 L_g$) and shunt (120 Mvar at PCC). These passive components are simplified as inductors. The values of L_g will be changed to analyze different SCR conditions in Section IV. Based on the reactive power of the shunt in Fig. 1, the real value of the shunt inductance is

$$L_{120(\mathrm{r})} = \frac{(220\ \mathrm{kV})^2}{2\pi \times 50\ \mathrm{Hz} \times 120\ \mathrm{Mvar}}. \tag{19}$$

The per-unit value is $L_{120(\mathrm{r})}$ over the base inductance at HV-side of transformer $\mathrm{T_I}$ in TABLE I. The impedance models should be in *dq*-frame, e.g., the grid impedance is

$$\boldsymbol{Z}_{\boldsymbol{g}}(s) = L_g\begin{bmatrix} s & -\omega_1 \\ \omega_1 & s\end{bmatrix}. \tag{20}$$

Then, the grid admittance $\boldsymbol{Y}_{\boldsymbol{g}}(s)$ equals to the inverse matrix of $\boldsymbol{Z}_{\boldsymbol{g}}(s)$, which is calculated numerically by Matlab. The shunt $\boldsymbol{Y}_{120}(s)$ is the same but with different inductance value.

2) Offshore WPP transformer $\mathrm{T_{II}}$. This is an aggregated transformer that links the WPP to the transmission. The transformer $\mathrm{T_{II}}$ is modeled as equivalent leakage inductance L_T and resistance R_T for simplicity, where their detailed values are listed in TABLE I. Thus, in *dq*-frame, the impedance of $\mathrm{T_{II}}$ is given as

$$\boldsymbol{Z}_{\boldsymbol{T}}(s) = \begin{bmatrix} R_T + sL_T & -\omega_1 L_T \\ \omega_1 L_T & R_T + sL_T\end{bmatrix}. \tag{21}$$

3) Transmission network from bus $\mathrm{B_I}$ (high-voltage side of $\mathrm{T_{II}}$) to PCC. This is a two-port network containing long cables and shunts. The traditional cable models in [32] are hard to capture the accurate dynamics with multiple resonances. Therefore, this study applies the black-box modeling in simulations as shown in Fig. 4 to simplify the complex derivation with satisfying accuracy. A typical flow of the two-port black-box modeling is: i) frequency scans at both ports; ii) transform to an equivalent PI-section in Fig. 4; iii) vector fitting (VF) of transfer functions. To be detailed, the frequency scans from two ports are performed in simulations to build the terminal characteristics. The

measurements are conducted four times – each port two times by setting $v_1 = 0$ and $v_2 = 0$ in Fig. 4 (connect to the ground). Then the admittance of the two-port network can be measured and calculated by

$$\begin{bmatrix} Y_{11} & Y_{12} \\ Y_{21} & Y_{22} \end{bmatrix} = \begin{bmatrix} \left.\frac{i_1(f)}{v_1(f)}\right|_{v_2=0} & \left.\frac{i_1(f)}{v_2(f)}\right|_{v_1=0} \\ \left.\frac{i_2(f)}{v_1(f)}\right|_{v_2=0} & \left.\frac{i_2(f)}{v_2(f)}\right|_{v_1=0} \end{bmatrix}. \quad (22)$$

In this passive network, Y_{12} equals to -Y_{21}. Next, the two-port network is transformed into an equivalent PI-section in Fig. 4, that is described as

$$\begin{cases} Y_{T1} = Y_{11} - Y_{12} \\ Y_{T2} = Y_{12} \\ Y_{T3} = Y_{22} - Y_{12} \end{cases}. \quad (23)$$

In this way, the network can be easily integrated with other components. The frequency scans are conducted in PSCAD/EMTDC from 1 Hz to 3 kHz, and the bode plots of the PI-section model are depicted in Fig. 5. Finally, the VF algorithm [34] in Matlab is utilized to obtain the *s*-domain transfer functions of the black-box model based on the data shown in Fig. 5. The frequency response of VF can be expressed as a sum of partial fractions [35], i.e.,

$$\boldsymbol{f}(s) = \sum_{m=1}^{N} \frac{\boldsymbol{c}_m}{s - a_m} + \boldsymbol{d} + s\boldsymbol{e}. \quad (24)$$

where N stands for the number of poles, $\boldsymbol{c}_m$ and a_m are the residues and poles, $\boldsymbol{d}$ and $\boldsymbol{e}$ are optional. In this study, N = 18 is enough for accuracy, and the error is around 2%.

4) Aggregated GFL converter (WPP). Fig. 6 shows the block diagram of the GFL control as well as PLL for WPP. The power control (APC and RPC) in Fig. 6 applies PI controller, i.e.,

$$C_A(s) = k_{pp} + k_{pi}/s. \quad (25)$$

$L_V(s)$ is an LPF for voltage feedforward. The current controller is a proportion gain k_p. The PLL also uses a PI controller, which is designed as [36]

$$C_L(s) = \omega_c + \omega_c \alpha_{ip}/s \quad (26)$$

where ω_c is the proportional gain, which denotes the PLL bandwidth [36]. α_p is chosen as $\omega_c/5$. The small-signal models of GFL control in Fig. 6 are well developed in [21], [31]. This study applies the same *dq*-frame impedance model in [31], expressed as $\boldsymbol{Z}_{\mathbf{GFL}}(s)$ in following figures.

B. Equivalent impedance modeling

After all the impedance/admittance models are obtained, the network is replotted in the first block of Fig. 7, which gives an overview of how the subsystems are integrated together from step 3) to 5). Then in step 3.2), the equivalent impedance model of the network $\boldsymbol{Z}_{\boldsymbol{E}}(s)$ seen from the PCC is calculated based on the series-parallel relations of the components, i.e.,

$$\boldsymbol{Z}_{\boldsymbol{E}}(s) = \{[\boldsymbol{Z}_{\boldsymbol{E}1}(s) + \boldsymbol{Y}_{\boldsymbol{T}2}^{-1}(s)]^{-1} + \boldsymbol{Y}_{\boldsymbol{T}1}(s) + \boldsymbol{Y}_{\boldsymbol{g}}(s) + \boldsymbol{Y}_{120}(s)\}^{-1} \quad (27)$$

where

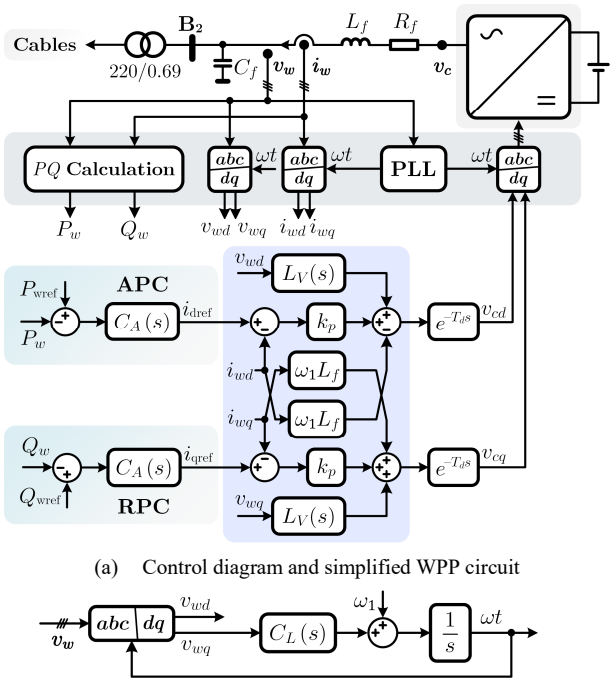

(a) Control diagram and simplified WPP circuit

(b) Block diagram of PLL

Fig. 6. Block diagram of the GFL control.

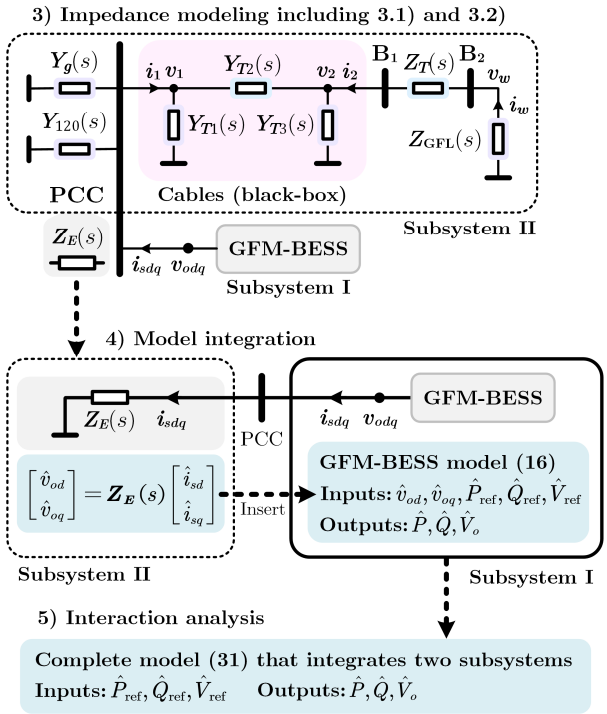

Fig. 7. Overview of modeling flow in Fig. 2 from step 3) to step 5).

$$\boldsymbol{Z}_{\boldsymbol{E}1}(s) = \{[\boldsymbol{Z}_{\mathbf{GFL}}(s) + \boldsymbol{Z}_{\boldsymbol{T}}(s)]^{-1} + \boldsymbol{Y}_{\boldsymbol{T}3}(s)\}^{-1}. \quad (28)$$

As a result, the network including WPPs and black-box transmission models is represented by an equivalent impedance model (transfer functions matrix) $\boldsymbol{Z}_{\boldsymbol{E}}(s)$, which contains the dynamics of GFL control as well as the passive network.

V. Model Integration

In step 4), $\boldsymbol{Z}_{\boldsymbol{E}}(s)$ in (27) will be integrated with the GFM-BESS model (17). According to the diagram in step 4) of Fig.

7, the terminal characteristics at PCC that link the two subsystems are expressed as

$$\hat{\boldsymbol{u}}_{\boldsymbol{v}} = \boldsymbol{Z}_{\boldsymbol{E}}(s)\hat{\boldsymbol{x}} = \boldsymbol{Z}_{\boldsymbol{E}}(s)\begin{bmatrix}\hat{i}_{sd} & \hat{i}_{sq}\end{bmatrix}^T \tag{29}$$

where $\hat{\boldsymbol{u}}_{\boldsymbol{v}}$ and $\hat{\boldsymbol{x}}$ are given in (12). Then substituting (29) into (17), the system model is derived as

$$\begin{aligned} s\hat{\boldsymbol{x}} &= \boldsymbol{A}_{\mathbf{sys}}(s)\hat{\boldsymbol{x}} + \boldsymbol{B}_{\mathbf{sys}}(s)\hat{\boldsymbol{u}}_{\mathbf{ref}} \\ \hat{\boldsymbol{y}} &= \boldsymbol{C}_{\mathbf{sys}}(s)\hat{\boldsymbol{x}} \end{aligned} \tag{30}$$

where

$$\begin{aligned} &\boldsymbol{A}_{\mathbf{sys}}(s) = \boldsymbol{A}_{\mathbf{GFM}}(s) + \frac{1}{L_{eq}}[-\boldsymbol{I}_{2\times 2} - \boldsymbol{B}_{\boldsymbol{s}}\boldsymbol{G}_{\boldsymbol{c}}(s)\boldsymbol{D}]\boldsymbol{Z}_{\boldsymbol{E}}(s) \\ &\boldsymbol{B}_{\mathbf{sys}}(s) = \frac{1}{L_{eq}}\boldsymbol{B}_{\boldsymbol{s}}\boldsymbol{G}_{\boldsymbol{c}}(s),\ \boldsymbol{C}_{\mathbf{sys}}(s) = \boldsymbol{C} + \boldsymbol{D}\boldsymbol{Z}_{\boldsymbol{E}}(s). \end{aligned} \tag{31}$$

(30) contains all components in Fig. 1. Finally, the control reference-to-output transfer function model is given as

$$\frac{\hat{\boldsymbol{y}}}{\hat{\boldsymbol{u}}_{\mathbf{ref}}} = \boldsymbol{C}_{\mathbf{sys}}(s)\left[s\boldsymbol{I} - \boldsymbol{A}_{\mathbf{sys}}(s)\right]^{-1}\boldsymbol{B}_{\mathbf{sys}}(s) \tag{32}$$

where the input $\hat{\boldsymbol{u}}_{\mathbf{ref}}$ and output $\hat{\boldsymbol{y}}$ are given in (6) and Fig. 7. The model (32) describes the dynamic behaviors of the control references including power and voltage magnitude to outputs. It contains the coupling effects between different loops and components. Thus, the dynamic interactions for controller tuning in various conditions, e.g., SCRs, can be performed based on the model. The stability evaluation and sensitivity analysis can also be conducted by checking the poles of $\boldsymbol{C}_{\mathbf{sys}}(s)\left[s\boldsymbol{I} - \boldsymbol{A}_{\mathbf{sys}}(s)\right]^{-1}\boldsymbol{B}_{\mathbf{sys}}(s)$ [33].

VI. EMT Verification and Interactions Analysis

The main circuit and controller parameters of the studied system are listed in TABLE I and II. The per-unit value calculation is given in [36], but please note the base frequency in this study is set as $\omega_{\text{base}} = 1$ rad/s. The long cable network is obtained as a black-box model presented in Section IV–A. The measured maximum SCR (L_g = 0) for the offshore WPP is 3.7. The onshore grid impedance L_g will increase from 0 to emulate different cases (SCR = 3.7~1.7).

In this section, the EMT verification of the reference-to-output transfer function matrix (32) is given first. Then, the dynamic interactions of GFM control loops and WPPs are analyzed in different cases based on the bode plots. Finally, the controller parameter-dependent interactions are studied by the sensitivity analysis. The delivered information and conclusions will be summarized in the end.

A. EMT verification

The step responses of reference-to-output model in Matlab and EMT simulation waveforms in PSCAD are presented in Fig. 8. The P_{ref} to P responses are given in Fig. 8(a), where a small step (0.9%) is performed on the reference. The model (wider blue line) shows almost identical results as the EMT simulations, indicating high accuracy. Fig. 8(b) shows an evident coupling ripple on P when V_{ref} changes from 1 p.u. to 0.98 p.u., and the model is also very closed to the EMT result. Similarly, when reference P_{ref} changes, coupling effects on output voltage magnitude V_o is also observed in Fig. 8(c), where very small errors exist around 0.05~0.15 s. Finally, the step responses of V_{ref} to V_o indicate satisfying accuracy too.

TABLE I.
MAIN CIRCUIT PARAMETERS

Parameter	Base value	Per-unit value
Circuit parameters of offshore WPP		
Rated voltage V_{nl}	0.69 kV (L-L RMS)	1 p.u.
Rated capacity S_{nl}	444 MVA	1 p.u.
Rated active power P_{nl}	400 MW	1 p.u.
Nominal frequency ω_1	1 rad/s	314 p.u.
Filter inductance L_f	1.072 mH	0.12/314 p.u.
Inductor ESR R_f	1.072 mΩ	0.01 p.u.
Filter capacitance C_f	1.072 mF	0.02/314 p.u.
Circuit parameters of GFM-BESS		
Rated voltage V_{nm}	33 kV (L-L RMS)	1 p.u.
Rated capacity S_{nm}	112 MVA	1 p.u.
Rated active power P_{nm}	50 MW	1 p.u.
Filter inductance L_s	9.723 H	0.1/314 p.u.
Filter ESR R_s	9.723 Ω	0.005 p.u.
Onshore grid		
Rated voltage V_{on}	220 kV (L-L RMS)	1 p.u.
Transformer T_{II} of offshore WPP		
Primary voltage V_{pl}	220 kV (L-L RMS)	1 p.u.
Secondary voltage V_{sl}	0.69 kV (L-L RMS)	1 p.u.
Rated capacity S_{tl}	450 MVA	1 p.u.
Leakage inductance L_T	107.6 H (HV-side)	0.08/314 p.u.
Copper loss R_T	107.6 Ω (HV-side)	0.002 p.u.
Transformer T_I of GFM-BESS		
Primary voltage V_{pm}	220 kV (L-L RMS)	1 p.u.
Secondary voltage V_{sm}	33 kV (L-L RMS)	1 p.u.
Rated capacity S_{tm}	112 MVA	1 p.u.
Leakage inductance L_l	432.1 H (HV-side)	0.1/314 p.u.
Copper loss R_l	432.1 Ω (HV-side)	0.002 p.u.

TABLE II
MAIN CONTROL PARAMETERS

GFL control parameters of offshore WPPs		
PLL bandwidth	ω_c	10π rad/s
Current controller (CC)	k_p	1.2 p.u.
Power controller (PC)	k_{pp}	0.5 p.u.
	k_{pi}	140 p.u.
Control delay	T_{dl}	250 μs
GFM control parameters of BESS		
PSC controller	k_{si}	$0.016\omega_1$ p.u.
	ω_p	20π rad/s
AVC controller	k_{ei}	20 p.u.
	ω_v	20π rad/s
VR controller	R_a	0.1 p.u.
	α_c	10π rad/s

B. Transfer function-based interactions analysis

Based on the reference-to-output transfer function matrix, the dynamic interactions between control loops, GFM-BESS and offshore WPPs are analyzed in different cases.

Fig. 9 shows the frequency responses of the model when SCR decreases from 3.7 to 1.7 (L_g increases). Fig. 9(a) gives the control dynamics of PSC from P_{ref} to P, where the control bandwidth decreases with lower SCRs. This conclusion can be verified by the EMT simulation in Fig. 10(a).

The coupling effect from V_{ref} to P is depicted in Fig. 9(b). The frequency responses in 1~10 Hz range are over 0 dB, and the coupling is more obvious in stronger grid, which is proven by EMT step responses in Fig. 10(b).

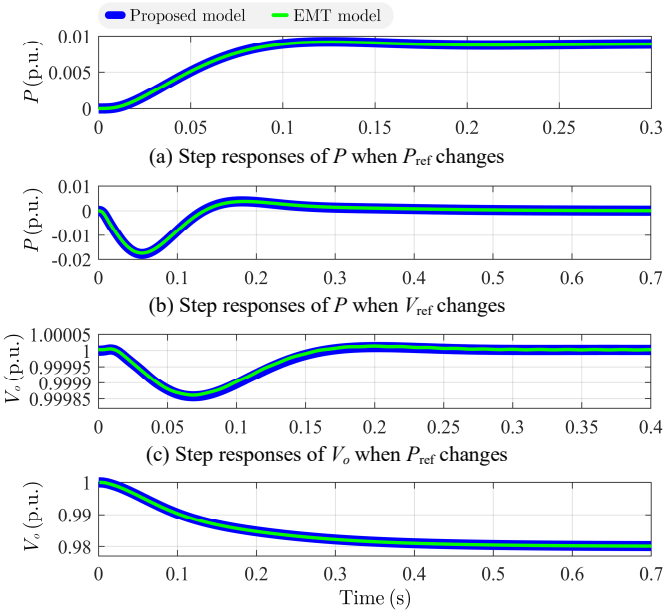

(a) Step responses of P when P_{ref} changes

(b) Step responses of P when V_{ref} changes

(c) Step responses of V_o when P_{ref} changes

(d) Step responses of V_o when V_{ref} changes

Fig. 8. Step responses of the proposed model and EMT simulation.

Similarly, the coupling effect from P_{ref} to V_o is given in Fig. 9(c). The output voltage V_o is more robust in comparison with P in Fig. 9(b), and the magnitudes are smaller than -30 dB in all frequency ranges. Hence, the couplings can be neglected, though it shows an opposite rule when decreasing SCRs as Fig. 9(b), which are verified in Fig. 10(c).

The dynamics of AVC from V_{ref} to V_o are shown in Fig. 9(d). The AVC bandwidth increases with lower SCRs, which is opposite to PSC, and the bandwidth variation is quite obvious. These features can also be proven by simulations in Fig. 10(d).

Fig. 11 presents the frequency responses of the model when the active power of WPP P_w increases from 0 to 1 p.u. It directly reflects the interactions between WPP and GFM-BESS. Fig. 11(a) depicts the control dynamics of PSC from P_{ref} to P. The PSC bandwidth slightly increases with higher active power of the WPP, which is validated by simulation results in Fig. 12(a). Fig. 11(b) illustrates the control dynamics of AVC from V_{ref} to V_o. It shows similar rules as PSC, and the EMT verification is shown in Fig. 12(b). As for the coupling effects, the influences are much smaller, thus are neglected.

Fig. 13 shows the frequency responses when the active power of GFM-BESS P increases from -1 to 1 p.u. The directions of P also influence the control dynamics. Fig. 13(a) shows the coupling from V_{ref} to P, and the magnitude definitely grows with higher generated active power of GFM-BESS. Similar coupling effects from P_{ref} to V_o in Fig. 13(b) can also be observed, but the magnitudes are much smaller. These features are verified by the simulation results in Fig. 14. As for the diagonal PSC and AVC dynamics, the influence of steady-state points of P is not obvious, thus not presented in this study.

In summary, the following information can be delivered based on the analysis above:

1) The highest bandwidth of PSC will be identified in the case with the strongest grid and the highest active power generation of WPP. The integral gain k_{si} of PSC as well as the VR needs to be tuned in this case to avoid potential resonance near 50 Hz. On the contrary, the AVC shows an evident bandwidth growth in weaker grids.
2) In comparison with the offshore WPP, the grid is much stronger for the onshore GFM-BESS, since its capacity is much lower and it is closer to the main grid. In this case, the voltage reference-to-power coupling is quite obvious, especially with higher SCR and power. A compromise solution is to reduce the AVC bandwidth to mitigate the undesirable coupling. By contrast, the voltage magnitude showcases a more robust profile, hence the coupling from active power can be neglected in the controller tuning.

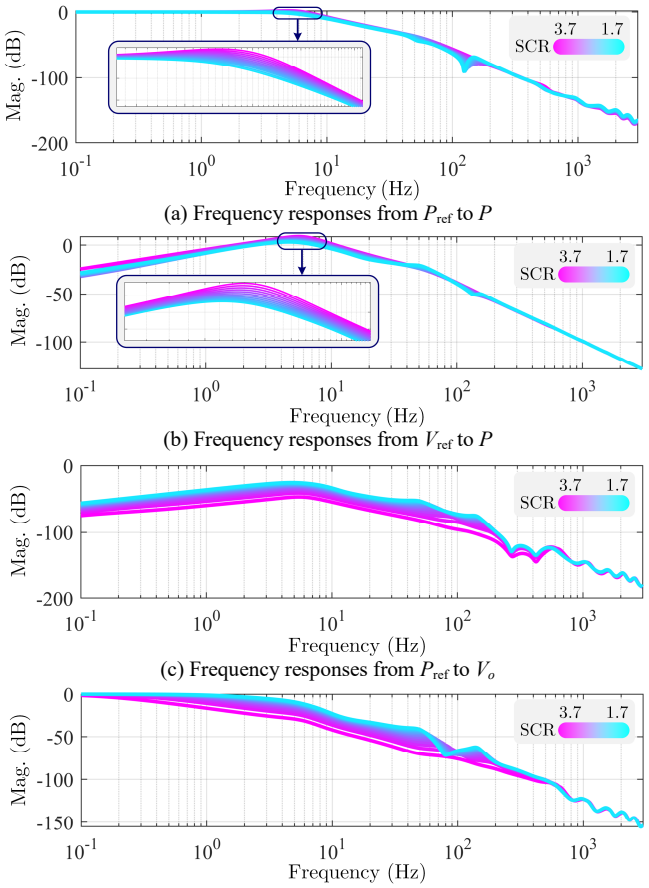

(a) Frequency responses from P_{ref} to P

(b) Frequency responses from V_{ref} to P

(c) Frequency responses from P_{ref} to V_o

(d) Frequency responses from V_{ref} to V_o

Fig. 9. Frequency responses of GFM-BESS when SCR decreases (3.7~1.7).

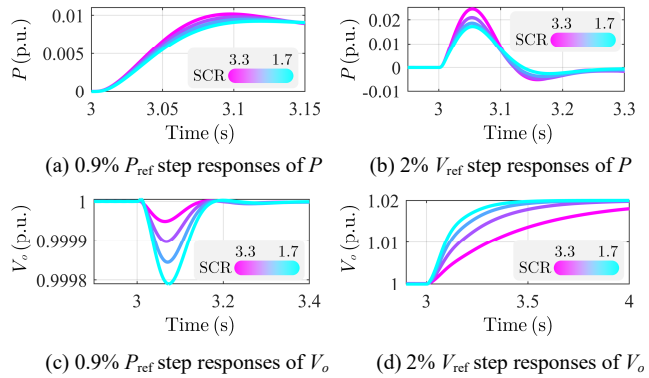

(a) 0.9% P_{ref} step responses of P

(b) 2% V_{ref} step responses of P

(c) 0.9% P_{ref} step responses of V_o

(d) 2% V_{ref} step responses of V_o

Fig. 10. EMT step responses when SCR decreases (3.7~1.7).

C. *Sensitivity-based interaction analysis*

Two poles are focused in this study, which are respectively

This article has been accepted for publication in a future issue of this journal, but has not been fully edited. Content may change prior to final publication. Citation information: DOI 10.1109/TPWRS.2021.3096850, IEEE Transactions on Power Systems

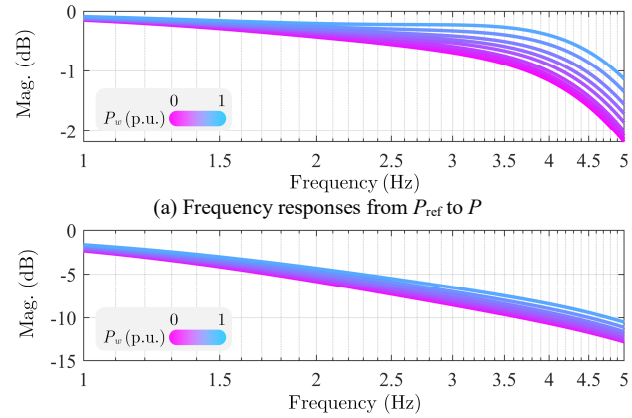

(a) Frequency responses from P_{ref} to P

(b) Frequency responses from V_{ref} to V_o

Fig. 11. Frequency responses of GFM-BESS when active power of offshore WPP increases (0~1 p.u.).

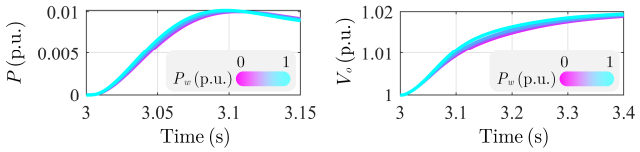

(a) 0.9% P_{ref} step responses of P (b) 2% V_{ref} step responses of V_o

Fig. 12. EMT step responses when active power of WPP increases (0~1 p.u.).

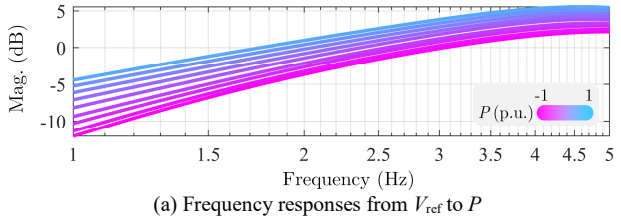

(a) Frequency responses from V_{ref} to P

(b) Frequency responses from P_{ref} to V_o

Fig. 13. Frequency responses of GFM-BESS when P increases (-1~1 p.u.).

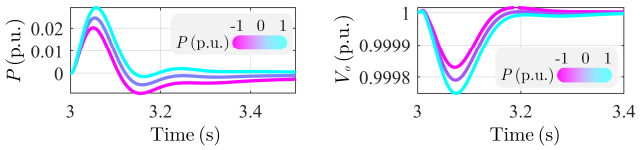

(a) 2% V_{ref} step responses of P (b) 0.9% V_{ref} step responses of P

Fig. 14. EMT step responses when P increases (-1~1 p.u.).

related to the low-frequency features of PLL in WPP and PSC in GFM-BESS. The identification of the two poles are given as follows: i) when the PLL bandwidth ω_c of WPP increases from the nominal value in TABLE II, a pair of poles will gradually move to the right-half-plane (RHP), hence they are defined as λ_{PLL}; ii) when the PSC integral gain k_{si} of GFM-BESS increases from the nominal value in TABLE II, another pair of poles will gradually move to the RHP, thus they are identified as λ_{PSC}. The following analysis will investigate the interactions between the WPP and GFM-BESS based on λ_{PLL} and λ_{PSC} that characterize the GFL and GFM dynamics.

Fig. 15 depicts λ_{PLL} when SCR decreases. λ_{PLL} evidently moves to the right in weaker grids, indicating undesirable

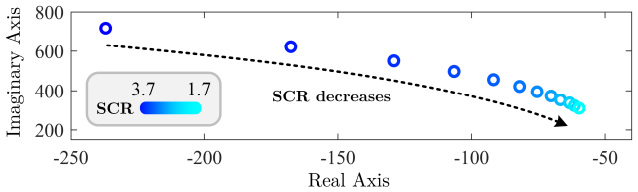

Fig. 15. Comparisons of λ_{PLL} when SCR decreases (from 3.7 to 1.7).

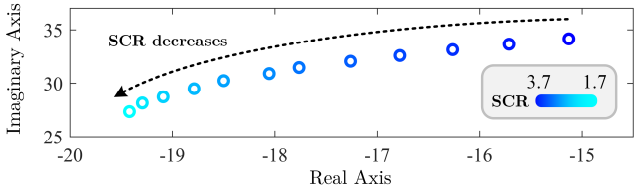

Fig. 16. Comparisons of λ_{PSC} when SCR decreases (from 3.7 to 1.7).

stability performances of GFL-based offshore WPP. In contrast, Fig. 16 presents the λ_{PSC} when SCR decreases, and λ_{PSC} moves to the left with lower SCRs, bringing more stability margin. This phenomenon indicates that the PSC is indeed suitable for the weak grid operation [15], [29].

Sensitivity analysis is performed for the damping ratios of λ_{PLL} and λ_{PSC} to evaluate the interactions regarding to different control parameters of WPP and GFM-BESS as well as SCRs. The damping ratios (ζ_{PLL} of λ_{PLL}, ζ_{PSC} of λ_{PSC}) can be obtained from pole-zero plots by the model, then the sensitivity (taking λ_{PLL} as an example) is calculated as [26]

$$\frac{\partial \zeta_{PLL}}{\partial k_i} \approx \frac{\zeta_{PLL}(k_{i0}+\Delta k_i)-\zeta_{PLL}(k_{i0})}{\Delta k_i} \tag{33}$$

where k_i is the ith parameter (k_p, k_{pp}, ω_c, ...), k_{i0} denotes its original value and Δk_i is 5% of k_{i0}. A screening method [37] is applied based on (33) to provide more insights from the analysis, i.e., the calculation in (33) is performed for different original values k_{i0} (10 points within 50~150%) of each parameter, then the average value and standard deviation [37] (representing non-linearity) for the 10 points are obtained. The results are shown in the heatmaps for λ_{PLL} and λ_{PSC} from Fig. 17 to Fig. 20. The positive value indicates when the parameters increase, the damping ratios grow. The following knowledge can be delivered from the heatmaps.

1) The virtual resistance R_a provides evident positive damping to the WPP λ_{PLL} in Fig. 17, whereas it shows opposite influence on the GFM-BESS λ_{PSC} in Fig. 18. This trade-off limits the damping effect of VR.
2) In comparison with PLL bandwidth ω_c, the proportional gains of current and power controller (k_p and k_{pp}) are more sensitive to λ_{PLL} in Fig. 17, while they all indicate small influences on λ_{PSC} of the GFM-BESS in Fig. 18.
3) The SCR shows opposite damping effects on λ_{PLL} and λ_{PSC} in Fig. 17 and 18, and indicates the strongest non-linearity in Fig. 19 and 20. Please note that the capacity of onshore GFM-BESS is normally much lower than offshore WPP due to the cost of batteries. Hence, the SCR seen from the GFM-BESS is much higher than the one from the WPP. It is therefore suggested to tune and evaluate the GFM-BESS in a strong grid (high SCR) as the worst case due to the negative sensitivity of SCR in Fig. 18, rather than design and operate for a very weak grid.

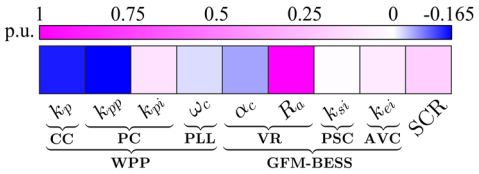

Fig. 17. Sensitivity analysis of average values for λ_{PLL}.

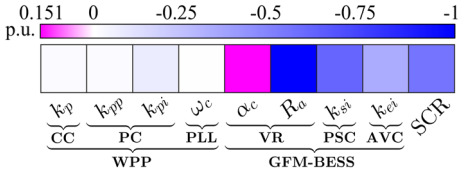

Fig. 18. Sensitivity analysis of average values for λ_{PSC}.

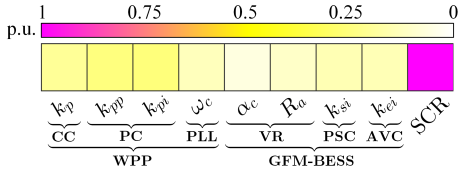

Fig. 19. Sensitivity analysis of standard deviations for λ_{PLL}.

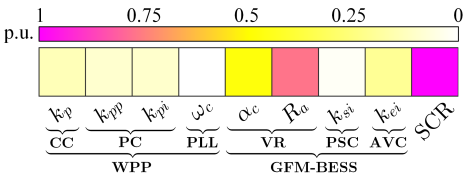

Fig. 20. Sensitivity analysis of standard deviations for λ_{PSC}.

VII. Conclusion

This paper presents a control interaction modeling and analysis method for the GFM-BESS with the offshore WPPs. The case analysis of the proposed model offers explicit insights of the interacted dynamic behaviors and identifies the critical controller parameters under different conditions. Some conclusions are summarized as follows.

1) The PSC bandwidth increases with higher SCRs and higher active power of the WPP. On the contrary, the AVC bandwidth decreases evidently in stronger grids. Since the grid is much stronger for the GFM-BESS in comparison with the WPP, the voltage reference-to-power coupling is quite obvious, thus lower AVC bandwidth is suggested. The power reference-to-voltage coupling, on the other hand, can be fully neglected in this case.
2) The virtual resistance of GFM-BESS showcases positive damping effects on the WPP, whereas it indicates opposite influences on the GFM-related poles. The SCR also has similar opposite effects. A strong grid for GFM-BESS is a typical condition in this application. Hence, the GFM-BESS control needs to be tuned and assessed in the highest SCR as the worst case rather than a traditional weak grid.
3) The proportional gains of current and power controllers of WPP as well as virtual resistance of GFM-BESS are actually more sensitive than the PLL bandwidth to the poles that related to PLL dynamics. In contrast, the GFM-BESS poles, which reflect the PSC dynamics, are much more robust to the WPP control parameters.

References

[1] Ł. H. Kocewiak, J. Hjerrild, and C. L. Bak, “Wind turbine converter control interaction with complex wind farm systems,” *IET Renewable Power Generation*, vol. 7, no. 4, pp. 380–389, Jul. 2013.

[2] E. Ebrahimzadeh, F. Blaabjerg, X. Wang and C. L. Bak, "Harmonic Stability and Resonance Analysis in Large PMSG-Based Wind Power Plants," *IEEE Trans. Sustain. Energy*, vol. 9, no. 1, pp. 12-23, Jan. 2018.

[3] Ł. H. Kocewiak, I. A. Aristi, B. Gustavsen and A. Hołdyk, "Modelling of wind power plant transmission system for harmonic propagation and small-signal stability studies," *IET Renewable Power Generation*, vol. 13, no. 5, pp. 717-724, Apr. 2019.

[4] C. Han, A. Q. Huang, M. E. Baran, S. Bhattacharya, W. Litzenberger, L. Anderson, A. L. Johnson and A. Edris, "STATCOM Impact Study on the Integration of a Large Wind Farm into a Weak Loop Power System," *IEEE Trans. Energy Conversion*, vol. 23, no. 1, pp. 226-233, Mar. 2008.

[5] L. Wang, C. Chang, B. Kuan and A. V. Prokhorov, "Stability Improvement of a Two-Area Power System Connected With an Integrated Onshore and Offshore Wind Farm Using a STATCOM," *IEEE Trans. Ind. Appl*., vol. 53, no. 2, pp. 867-877, Mar-Apr. 2017.

[6] M. Molinas, J. A. Suul and T. Undeland, "Low Voltage Ride Through of Wind Farms With Cage Generators: STATCOM Versus SVC," *IEEE Trans. Power Electron*., vol. 23, no. 3, pp. 1104-1117, May. 2008.

[7] A. Moharana, R. K. Varma and R. Seethapathy, "SSR Alleviation by STATCOM in Induction-Generator-Based Wind Farm Connected to Series Compensated Line," *IEEE Trans. on Sustainable Energy*, vol. 5, no. 3, pp. 947-957, Jul. 2014.

[8] N. Mendis, K. M. Muttaqi and S. Perera, "Management of Low- and High-Frequency Power Components in Demand-Generation Fluctuations of a DFIG-Based Wind-Dominated RAPS System Using Hybrid Energy Storage," *IEEE Trans. Ind. Appl*., vol. 50, no. 3, pp. 2258-2268, May-Jun. 2014.

[9] S. M. Muyeen, R. Takahashi, T. Murata, J. Tamura, and Mohd. H. Ali, “Application of STATCOM/BESS for wind power smoothening and hydrogen generation,” *Electric Power Systems Research*, vol. 79, no. 2, pp. 365–373, Feb. 2009.

[10] S. W. Mohod and M. V. Aware, "A STATCOM-Control Scheme for Grid Connected Wind Energy System for Power Quality Improvement," *IEEE Systems Journal*, vol. 4, no. 3, pp. 346-352, Sept. 2010.

[11] J. Z. Zhou, H. Ding, S. Fan, Y. Zhang, and A. M. Gole, “Impact of Short-Circuit Ratio and Phase-Locked-Loop Parameters on the Small-Signal Behavior of a VSC-HVDC Converter,” *IEEE Trans. Power Del.*, vol. 29, no. 5, pp. 2287–2296, Oct. 2014.

[12] S. K. Chaudhary, R. Teodorescu, Ł. H. Kocewiak, P. Johnson, C. Y. Chen, B. Berggren and L. Harnefors, “Challenges in Integration of MMC STATCOM with Battery Energy Storage for Wind Power Plants,” *18th Int'l Wind Integration Workshop*, Dublin, Ireland, pp. 1-5, Oct. 2019.

[13] S. Cherevatskiy, S. Zabihi, R. Korte, H. Klingenberg, S. Sproul, J. Glassmire, B. Buchholz and H. Bitaraf, "A 30MW Grid Forming BESS Boosting Reliability in South Australia and Providing Market Services on the National Electricity Market," *18th Int'l Wind Integration Workshop*, Dublin, Ireland, pp. 1-8, Oct. 2019.

[14] G. Li, Y. Chen, A. Luo, and H. Wang, “An Enhancing Grid Stiffness Control Strategy of STATCOM/BESS for Damping Sub-Synchronous Resonance in Wind Farm Connected to Weak Grid,” *IEEE Trans. Ind. Inf.*, vol. 16, no. 9, pp. 5835–5845, Sep. 2020.

[15] H. Wu and X. Wang, “Design-Oriented Transient Stability Analysis of Grid-Connected Converters With Power Synchronization Control,” *IEEE Trans. Ind. Electron.*, vol. 66, no. 8, pp. 6473–6482, Aug. 2019.

[16] S. K. Chaudhary, X. Wang, D. Yang, R. Teodorescu, Ł. H. Kocewiak, M. P. S. Gryning and C. Y. Chen, “Techno-economic Feasibility of a STATCOM with Battery Energy Storage for the Offshore Wind Power Plants,” *In Proceedings of the CIGRE Symposium Aalborg 2019*, Aalborg, Denmark, Jun. 2019.

[17] High Penetration of Power Electronic Interfaced Power Sources and the Potential Contribution of Grid Forming Converters, ENTSO-E technical report, Jan. 2020.

[18] J. Fang, Y. Tang, H. Li and X. Li, "A Battery/Ultracapacitor Hybrid Energy Storage System for Implementing the Power Management of Virtual Synchronous Generators," *IEEE Trans. Power Electron*., vol. 33, no. 4, pp. 2820-2824, Apr. 2018.

[19] A. Rahmoun, A. Armstorfer, H. Biechi, and A. Rosin, “Mathematical modeling of a battery energy storage system in grid forming mode,” IEEE 58th International Scientific Conference on Power and Electrical Engineering of Riga Technical University, Latvia, pp. 1–6, Oct. 2017.

[20] K. M. Alawasa and Y. A. I. Mohamed, "Impedance and Damping Characteristics of Grid-Connected VSCs With Power Synchronization Control Strategy," *IEEE Trans. Power Syst*., vol. 30, no. 2, pp. 952-961, Mar. 2015.
[21] X. Wang, L. Harnefors, and F. Blaabjerg, "Unified impedance model of grid-connected voltage-source converters," *IEEE Trans. Power Electron.*, vol. 33, no. 2, pp. 1775–1787, Feb. 2018.
[22] H. Liu, X. Xie, and W. Liu, "An Oscillatory Stability Criterion Based on the Unified dq-Frame Impedance Network Model for Power Systems with High-Penetration Renewables," *IEEE Trans. Power Syst.*, vol. 33, no. 3, pp. 3472–3485, May. 2018.
[23] N. Pogaku, M. Prodanovic and T. C. Green, "Modeling, Analysis and Testing of Autonomous Operation of an Inverter-Based Microgrid," *IEEE Trans. Power Electron*., vol. 22, no. 2, pp. 613-625, Mar. 2007.
[24] J. Guo, T. Chen, B. Chaudhuri and S. Y. R. Hui, "Stability of Isolated Microgrids With Renewable Generation and Smart Loads," *IEEE Trans. on Sustainable Energy*, vol. 11, no. 4, pp. 2845-2854, Oct. 2020.
[25] R. Rosso, S. Engelken, and M. Liserre, "Robust Stability Investigation of the Interactions Among Grid-Forming and Grid-Following Converters," *IEEE J. Emerg. Sel. Topics Power Electron*., vol. 8, no. 2, pp. 991–1003, Jun. 2020.
[26] D. Yang and X. Wang, "Unified modular state-space modeling of grid-connected voltage-source converters," *IEEE Trans. Power Electron*., vol. 35, no. 9, pp. 9702–9717, Sept. 2020.
[27] L. Zhang, L. Harnefors and H. Nee, "Power-Synchronization Control of Grid-Connected Voltage-Source Converters," *IEEE Trans. Power Syst.*, vol. 25, no. 2, pp. 809-820, May. 2010.
[28] H. Zhang, L. Harnefors, X. Wang, J. P. Hasler, S. Ostlund, C. Danielsson and H. Gong, "Loop-at-a-Time Stability Analysis for Grid-Connected Voltage-Source Converters," *IEEE J. Emerg. Sel. Topics Power Electron*., early access, doi: 10.1109/JESTPE.2020.3024103.
[29] L. Zhang, "Modeling and control of VSC-HVDC links connected to weak AC systems," *Ph.D. dissertation*, KTH, Stockholm, Sweden, 2011.
[30] L. Harnefors, M. Hinkkanen, U. Riaz, F. M. M. Rahman and L. Zhang, "Robust Analytic Design of Power-Synchronization Control," *IEEE Trans. Ind. Electron.*, vol. 66, no. 8, pp. 5810-5819, Aug. 2019.
[31] B. Wen, D. Boroyevich, R. Burgos, P. Mattavelli, and Z. Shen, "Analysis of D-Q Small-Signal Impedance of Grid-Tied Inverters," *IEEE Trans. Power Electron*., vol. 31, no. 1, pp. 675–687, Jan. 2016.
[32] P. Kundur, N. J. Balu, and M. G. Lauby, Power system stability and control. McGraw-hill New York, 1994.
[33] S. Skogestad and I. Postlethwaite, Multivariable feedback control: analysis and design. Wiley New York, 2007.
[34] B. Gustavsen, "Improving the pole relocating properties of vector fitting," *IEEE Trans. Power Del.*, vol. 21, no. 3, pp. 1587-1592, Jul. 2006.
[35] B. Gustavsen and A. Semlyen, "Rational approximation of frequency domain responses by vector fitting," *IEEE Trans. Power Del.*, vol. 14, no. 3, pp. 1052-1061, Jul. 1999.
[36] L. Harnefors, M. Hinkkanen, O. Wallmark, and A. G. Yepes, Control of voltage-source converters and variable-speed drives. Västerås, Sweden, 2014.
[37] K. N. Hasan, R. Preece and J. V. Milanović, "Priority Ranking of Critical Uncertainties Affecting Small-Disturbance Stability Using Sensitivity Analysis Techniques," *IEEE Trans. Power Syst.*, vol. 32, no. 4, pp. 2629-2639, Jul. 2017.

Fangzhou Zhao received his B.S. degree in Electrical Engineering and Automation from University of Electronic Science and Technology of China (UESTC), Chengdu, China, in 2014, and Ph.D. degree in Electrical Engineering from Xi'an Jiaotong University (XJTU), Xi'an, China, in 2019.

Since 2020, he has been with Department of Energy Technology, Aalborg University, Aalborg, Denmark, where he is currently a Postdoctoral Researcher. His research interests include modular multilevel converter, grid-forming control and grid emulation system.

Xiongfei Wang (S'10-M'13-SM'17) received the B.S. degree from Yanshan University, Qinhuangdao, China, in 2006, the M.S. degree from Harbin Institute of Technology, Harbin, China, in 2008, both in electrical engineering, and the Ph.D. degree in energy technology from Aalborg University, Aalborg, Denmark, in 2013.

From 2009 he has been with the Department of Energy Technology, Aalborg University, where he became an Assistant Professor in 2014, an Associate Professor in 2016, a Professor and Leader of Electronic Power Grid (eGrid) Research Group in 2018. He is also a Visiting Professor at KTH Royal Institute of Technology, Stockholm, Sweden, from 2020. His current research interests include modeling and control of power electronic converters and systems, stability and power quality of power-electronics-dominated power systems, high-power converters.

Dr. Wang serves as a Member-at-Large of Administrative Committee for the IEEE Power Electronics Society (PELS) in 2020-2022, a Co-Editor-in-Chief for the IEEE TRANSACTIONS ON POWER ELECTRONICS LETTERS, and as an Associate Editor for the IEEE JOURNAL OF EMERGING AND SELECTED TOPICS IN POWER ELECTRONICS (JESTPE). He was selected into Aalborg University Strategic Talent Management Program in 2016. He has received six Prize Paper Awards in the IEEE Transactions and conferences, the 2018 Richard M. Bass Outstanding Young Power Electronics Engineer Award, the 2019 IEEE PELS Sustainable Energy Systems Technical Achievement Award, the 2020 IEEE Power & Energy Society Prize Paper Award, the 2020 JESTPE Star Associate Editor Award, and the Highly Cited Researcher in the Web of Science in 2019-2020.

Zichao Zhou received the B.S. degree in electrical engineering and automation and the M.S. degree in electrical engineering from Harbin Institute of Technology, Harbin, China, in 2017 and 2019, respectively. He is currently working toward the Ph.D. degree in power electronic engineering in Aalborg University, Aalborg, Denmark. His research interests include the modeling and stability analysis of power electronics systems.

Lennart Harnefors (Fellow, IEEE) received the M.Sc., Licentiate, and Ph.D. degrees in electrical engineering from the Royal Institute of Technology (KTH), Stockholm, Sweden, and the Docent (D.Sc.) degree in industrial automation from Lund University, Lund, Sweden, in 1993, 1995, 1997, and 2000, respectively.

From 1994 to 2005, he was with Mälardalen University, Västerås, Sweden, from 2001 as a Professor of electrical engineering. From 2001 to 2005, he was, in addition, a part-time Visiting Professor of electrical drives with Chalmers University of Technology, Göteborg, Sweden.

In 2005, he joined ABB, HVDC Product Group, Ludvika, Sweden, where, among other duties, he led the control development of the first generation of multilevel-converter HVDC Light. In 2012, he joined ABB, Corporate Research, Västerås, where he was appointed as a Senior Principal Scientist in 2013. He is, in addition, a part-time Adjunct Professor of power electronics with KTH.

Dr. Harnefors is an Editor of the IEEE Journal of Emerging and Selected Topics in Power Electronics and an Associate Editor of IET Electric Power Applications. He was the recipient of the 2020 IEEE Modeling and Control Technical Achieved Award and was acknowledged as an outstanding reviewer of IEEE Transactions of Power Electronics in 2018. His research interests include control and dynamic analysis of power electronic systems, particularly grid-connected converters and ac drives.

Jan R. Svensson (S'96, M'99, SM'2020) has a Ph.D. degree and a D.Sc. degree (Docent) from Chalmers University of Technology, Göteborg, Sweden. From 1999 to 2009, he worked in ABB with R&D of HVDC transmission, STATCOMs and energy storages, especially design and control of Light-concept devices (HVDC and FACTS). Between 2009 and 2014, he was Program Manager for the global R&D program "Active grid infrastructure" at ABB Corporate Research. From 2014 to 2020, he was a Senior Principal Scientist on power electronics systems at ABB Power Grids Research. In addition to his current role as a Research Fellow at Hitachi ABB Power Grids Research, he is also an adjunct professor at Chalmers University of Technology since 2018. His interests include design and control of power electronics in power systems, power quality, storage technologies and renewable energy.

Łukasz Hubert Kocewiak holds BSc and MSc degrees in electrical engineering from Warsaw University of Technology as well as PhD degree from Aalborg University. Currently he is with Ørsted Offshore and is working as an R&D manager. He is a power system specialist within the area of design of electrical infrastructure in large offshore wind power plants. The main direction of his research is related to harmonics, stability and nonlinear dynamics in power electronics and power systems especially focused on wind power generation units. He is the author/co-author of more than 100 publications. He is a member of various working groups / activities within Cigré, IEEE, IEC.

Mikkel Peter Sidoroff Gryning holds an MSc degree in electrical engineering with focus on automation and control, and a PhD in power system control robustness analysis, both from the Technical University of Denmark. Currently working as a specialist in the turbine SCADA department of Ørsted Offshore in areas such as wind farm and wind turbine control systems, SCADA communication protocols and network design, and OT/IT security impact and implementation for control and monitoring.